



Kent Academic Repository

Ramachandran, R., Sil, Milan, Gorai, Prasanta, Meka, J. K., Sundararajan, Pavithraa, Lo, J.-I., Chou, S.-L., Wu, Y.-J., Janardhan, P., Cheng, B.-M. and others (2024) *Experimental and Computational Study of Ethanolamine Ices under Astrochemical Conditions*. *The Astrophysical Journal*, 975 (2). ISSN 1538-4357.

Downloaded from

<https://kar.kent.ac.uk/107677/> The University of Kent's Academic Repository KAR

The version of record is available from

<https://doi.org/10.3847/1538-4357/ad77c5>

This document version

Publisher pdf

DOI for this version

Licence for this version

CC BY (Attribution)

Additional information

Versions of research works

Versions of Record

If this version is the version of record, it is the same as the published version available on the publisher's web site. Cite as the published version.

Author Accepted Manuscripts

If this document is identified as the Author Accepted Manuscript it is the version after peer review but before type setting, copy editing or publisher branding. Cite as Surname, Initial. (Year) 'Title of article'. To be published in **Title of Journal**, Volume and issue numbers [peer-reviewed accepted version]. Available at: DOI or URL (Accessed: date).

Enquiries

If you have questions about this document contact ResearchSupport@kent.ac.uk. Please include the URL of the record in KAR. If you believe that your, or a third party's rights have been compromised through this document please see our [Take Down policy](https://www.kent.ac.uk/guides/kar-the-kent-academic-repository#policies) (available from <https://www.kent.ac.uk/guides/kar-the-kent-academic-repository#policies>).



CrossMark

Experimental and Computational Study of Ethanolamine Ices under Astrochemical Conditions

R. Ramachandran^{1,2}, Milan Sil^{3,4,2}, Prasanta Gorai^{5,6,2}, J. K. Meka¹, Pavithraa Sundararajan⁷, J.-I. Lo⁸, S.-L. Chou⁹, Y.-J. Wu⁹, P. Janardhan¹, B.-M. Cheng⁸, Anil Bhardwaj¹, Víctor M. Rivilla¹⁰, N. J. Mason¹¹, B. Sivaraman¹, and Ankan Das^{2,12}

¹ Physical Research Laboratory, Ahmedabad 380009, India; ragav.kasak@gmail.com, bhala@prl.res.in

² Institute of Astronomy Space and Earth Science, P 177, CIT Road, Scheme 7m, Kolkata 700054, West Bengal, India; ankan.das@gmail.com

³ Univ. Grenoble Alpes, CNRS, IPAG, 38000 Grenoble, France

⁴ Univ Rennes, CNRS, IPR (Institut de Physique de Rennes)—UMR 6251, F-35000 Rennes, France

⁵ Roseland Centre for Solar Physics, University of Oslo, PO Box 1029 Blindern, 0315 Oslo, Norway

⁶ Institute of Theoretical Astrophysics, University of Oslo, PO Box 1029 Blindern, 0315 Oslo, Norway

⁷ Department of Applied Chemistry and Institute of Molecular Sciences, National Chiao Tung University, Hsinchu, Taiwan

⁸ Department of Medical Research, Hualien Tzu Chi Hospital, Buddhist Tzu Chi Medical Foundation, Hualien, Taiwan

⁹ National Synchrotron Radiation Research Centre, Hsinchu, Taiwan

¹⁰ Centro de Astrobiología (CSIC-INTA), Ctra. de Ajalvir Km. 4, Torrejón de Ardoz, 28850 Madrid, Spain

¹¹ Centre for Astrophysics and Planetary Science, School of Physical Sciences, University of Kent, Canterbury, CT2 7NH, UK

¹² Max-Planck-Institute for extraterrestrial Physics, PO Box 1312 85741 Garching, Germany

Received 2024 March 25; revised 2024 August 30; accepted 2024 August 30; published 2024 November 1

Abstract

Ethanolamine (NH₂CH₂CH₂OH) has recently been identified in the molecular cloud G+0.693-0.027, situated in the SgrB2 complex in the Galactic center. However, its presence in other regions, and in particular in star-forming sites, is still elusive. Given its likely role as a precursor to simple amino acids, understanding its presence in the star-forming region is required. Here, we present the experimentally obtained temperature-dependent spectral features and morphological behavior of pure ethanolamine ices under astrochemical conditions in the 2–12 μm (MIR) and 120–230 nm (VUV) regions for the first time. These features would help in understanding its photochemical behavior. In addition, we present the first chemical models specifically dedicated to ethanolamine. These models include all the discussed chemical routes from the literature, along with the estimated binding energies and activation energies from quantum chemical calculations reported in this work. We have found that surface reactions CH₂OH + NH₂CH₂ → NH₂CH₂CH₂OH and NH₂ + C₂H₄OH → NH₂CH₂CH₂OH in warmer regions (60–90 K) could play a significant role in the formation of ethanolamine. Our modeled abundance of ethanolamine complements the upper limit of ethanolamine column density estimated in earlier observations in hot core/corino regions. Furthermore, we provide a theoretical estimation of the rotational and distortional constants for various species (such as HNCCO, NH₂CHCO, and NH₂CH₂CO) related to ethanolamine that have not been studied in existing literature. This study could be valuable for identifying these species in the future.

Unified Astronomy Thesaurus concepts: Astrochemistry (75); Pre-biotic astrochemistry (2079); Chemical abundances (224); Infrared spectroscopy (2285); Ice spectroscopy (2250); Molecular spectroscopy (2095); Molecular data (2259); Interstellar abundances (832)

1. Introduction

Nitrogen- and oxygen-bearing complex organic molecules (COMs) in the interstellar medium (ISM) are of substantial significance as they are considered the precursors to biomolecules such as amino acids and proteins. Ethanolamine (NH₂CH₂CH₂OH), also called 2-aminoethanol, glycinol or monoethanolamine, is a probable precursor of simple amino acids like glycine and alanine (S. L. Widicus et al. 2003; E. S. Wirstrom & P. Bergman 2007). Ethanolamine is also a phospholipid precursor, which could play a crucial role in the evolution of the first cellular membranes needed for the emergence of life on early Earth (V. M. Rivilla et al. 2021; M. Fiore et al. 2022). Though several amino acids, including glycine and alanine, have been discovered on meteorites (K. A. Kvenvolden et al. 1971; D. P. Glavin et al. 2010) and

comets (K. Altwegg et al. 2016), they have been elusive in the ISM (Y.-J. Kuan et al. 2003; M. R. Cunningham et al. 2007; P. A. Jones et al. 2007; A. Belloche et al. 2008). Amino acids in the ISM could be formed from protonated amino alcohols and formic acid under suitable conditions (P. Ehrenfreund et al. 2001). However, a theoretical calculation by P. Redondo et al. (2015) revealed that the activation barrier of this reaction presents a significant challenge under interstellar conditions.

V. M. Rivilla et al. (2021) analyzed molecular data from high-sensitivity, unbiased spectral surveys conducted by the Yebes 40 m and the IRAM 30 m telescopes. They successfully detected ethanolamine for the first time in the interstellar medium. This detection was made toward the molecular cloud G+0.693-0.027, located in the SgrB2 complex in the Galactic center. Previously, ethanolamine had been searched for in various star-forming regions, including several hot cores (S. L. Widicus et al. 2003; E. S. Wirstrom & P. Bergman 2007) and the prototypical hot corino IRAS 16293-2422 B (P. Nazari et al. 2024). Telescopes such as the Caltech Submillimeter Observatory, Owens Valley Radio Observatory, and Onsala 20 m were utilized in these



Original content from this work may be used under the terms of the [Creative Commons Attribution 4.0 licence](https://creativecommons.org/licenses/by/4.0/). Any further distribution of this work must maintain attribution to the author(s) and the title of the work, journal citation and DOI.

searches. Despite extensive efforts, ethanolamine remained undetected until it was identified by V. M. Rivilla et al. (2021). Before this identification, only upper bounds for its column density had been determined. Furthermore, V. M. Rivilla et al. (2021) formulated potential ice-phase formation pathways for ethanolamine based on previous works (V. Wakelam et al. 2015; M. Ruaud et al. 2016; S. V. Kameneva et al. 2017; T. Suzuki et al. 2018; S. A. Krasnokutski 2021). However, the formation pathways of interstellar ethanolamine are still poorly known.

Several ice processing experiments (P. Ehrenfreund et al. 2001; M. P. Bernstein et al. 2002; J. E. Elsila et al. 2007; M. Nuevo et al. 2008) designed to understand the amino acid formation from simple interstellar molecules have found several organic molecules, including ethanolamine, in the resulting residue (after hydrolysis).

Here, we conducted a comprehensive theoretical and experimental study to understand the formation of ethanolamine and its photochemical behavior. Our paper presents the first experimental results of the infrared (IR) and vacuum ultraviolet (VUV) study of pure ethanolamine ices under astrophysical conditions. Furthermore, we have developed a chemical model to study the fate of ethanolamine formation in hot core/corino regions.

The remainder of this paper is organized as follows: Section 2 discusses the implemented method for this study, Results and discussion are presented in Section 3, and the conclusions are summarized in Section 4.

2. Methodology and Computational Details

UV photons (including VUV) are ubiquitous in the ISM and play a vital role in its photochemistry (H. Carrascosa et al. 2020) and astronomical observations. Infrared spectroscopy is a valuable tool because the vibrational and rotational spectra of molecules could provide unique fingerprints that can be used to identify and characterize them. In interpreting interstellar ice's chemical composition, infrared spectra are invaluable. For example, the data gathered by the JWST are often analyzed by considering the comprehensive resources available in the Leiden Ice Database for Astrochemistry (W. R. M. Rocha et al. 2022). The VUV photoabsorption of astrochemical ices helps identify molecules by comparing data from spectra returned by spacecraft in the VUV region. For example, VUV spectroscopy of astrochemical ices facilitated the identification of hydrazine on Saturn's moon Rhea (M. Elowitz et al. 2021). In addition to these experimental studies, a coupled computational approach is needed to comprehend its formation and assess its abundance in interstellar circumstances. This section discusses the experimental and computational methods implemented in this work to study the fate of ethanolamine in interstellar conditions.

2.1. Experimental Studies

2.1.1. VUV Experiments

VUV photoabsorption experiments of ethanolamine ices were carried out with the VUV light from beamline BL-03 of the Taiwan Light Source at the National Synchrotron Radiation Research Centre (NSRRC), Taiwan. The VUV light from the synchrotron was incident normal to the sample, and the light hence transmitted was passed through a glass window coated with sodium salicylate to convert the incident UV light to

visible light and detect it using a photomultiplier tube (Hamamatsu R943-02), operating in a photon-counting mode. Detailed discussions of the experimental setup, liquid sample preparation, and spectral acquisition have been presented in earlier literature (H.-C. Lu et al. 2008). The ethanolamine molecules of high purity (>99% purity, Sigma Aldrich) were deposited on the LiF substrate at 10 K. The LiF substrate is chosen because it is UV transparent, especially in the regions of our interest. Upon deposition, a spectrum was recorded at 10 K. The sample was then heated to higher temperatures. After multiple experimental runs, we understand how the spectra change with temperature. Hence, we choose a convenient size that best captures these changes. A heating rate of 5 K minute⁻¹ is utilized, and upon stabilization at each 20 K interval, the spectrum is captured to analyze variations in VUV spectral signatures ranging from 120 to 230 nm. For all the experiments in VUV, the thickness used was ~20 ML.

2.1.2. IR Experiments

The temperature-dependent infrared spectroscopy of the ethanolamine ice was carried out using the Simulator for Astro-molecules at Low Temperature facility housed in the Physical Research Laboratory, Ahmedabad. The setup and other details are mentioned in R. Ramachandran et al. (2023).

Ethanolamine (>99 % purity, Sigma Aldrich), available as a liquid, was used. The sample was processed by several freeze-pump-thaw cycles. Due to its good vapor pressure at room temperature (0.54 mbar at 25°C), the usual deposition procedure (M. Elowitz et al. 2021; R. Ramachandran et al. 2023) was followed. In the first step of the experiment, the all-metal leak valve was opened in a controlled way to deposit the ethanolamine molecules on the ZnSe window, which was precooled to 7 K and subsequently monitored in situ using FTIR spectroscopy in the mid-IR range (4000–650 cm⁻¹). The ice was warmed then to higher temperatures with a ramp rate of 5 K min⁻¹, and the spectra were recorded at regular intervals of 5–10 K until its sublimation. Similar deposition procedures were followed for the deposition at different temperatures. For variable thicknesses, the deposition time was varied while monitoring the absorbance of the most prominent peak of the ice in the mid-IR region. In basic infrared experiments, an ice thickness of approximately 57 ML was employed.

2.2. Computational Studies

2.2.1. Binding Energies

One of the main challenges in accurately modeling interstellar chemistry is the limited knowledge of the binding energy (BE) of interstellar species. The abundances of these species are influenced by their adsorption and desorption on grains. While no previous literature on BEs was available for ethanolamine and related species, we are attempting for the first time to provide estimated values of BE. Ab initio quantum chemical calculations are carried out using Gaussian 09 and Gaussian 16 program packages (M. J. Frisch et al. 2013, 2016) to compute BEs for ethanolamine and related species having undefined BEs and noted in Table 1 along with the ground state spin multiplicities. Among several structural isomers of ethanolamine (Y. V. Novakovskaya & M. N. Rodnikova 2015), we consider the lowest-energy structure (g'Gg') for all our calculations. Water ice is the dominant component of the interstellar grain mantle in the

Table 1
ZPE-corrected BEs Considering Water Tetramer as a Substrate Using the MP2/aug-cc-pVDZ Level of Theory

Serial Number	Species	Ground State	ZPE-corrected Binding Energy (K)
1	HNCCO	singlet	3296
2	NH ₂ CCO	doublet	4935
3	NH ₂ CH	singlet	6119
4	CH ₂ OH	doublet	3864
5	C ₂ H ₄ OH	doublet	3656
6	NH ₂ CH ₂	doublet	2987
7	NH ₂ CHCO	singlet	2357
8	NH ₂ CH ₂ CO	doublet	3044
9	NH ₂ CH ₂ CHO	singlet	4314
10	NH ₂ CH ₂ CH ₂ O	doublet	3195
11	NH ₂ CH ₂ CHOH	doublet	4509
12	NH ₂ CH ₂ CH ₂ OH	singlet	4744

dense regions of ISM (A. C. A. Boogert et al. 2015). Though recent studies (A. Germain et al. 2022; L. Tinacci et al. 2022) suggest that a significant number (~ 100) of H₂O molecules in the amorphous solid water (ASW) cluster could simulate the realistic interstellar ice mantle, we assume the water c-tetramer structure to be a unit of ASW substrate (A. Das et al. (2018) showed it gives an average percentage deviation from the experiment of $\sim \pm 18.8\%$) and a single binding site despite having larger BE distribution (J. Heyl et al. 2022; M. Sil et al. 2024) due to a very high computational cost of computing BE distributions. The BE is typically considered a local property that results from the electronic interaction between the substrate (grain surface or adsorbent) and the species deposited on it (adsorbate). In the case of a bound adsorbate, the BE is a positive value. It is defined as the difference in the electronically optimized energy between the separated species and substrate and the adsorbed species on the substrate. The optimized energies of the species, water tetramer cluster, and complexes are calculated at the MP2/aug-cc-pVDZ level of theory (T. H. J. Dunning 1989). All the BE calculations are performed by optimizing every degree of freedom and using harmonic vibrational zero-point energy (ZPE) corrections to consider molecular vibration at low temperatures. It must be acknowledged that BE calculations are often far from simple approaches like this study and highly depend on the methodology used.

2.2.2. Chemical Reaction Rates

Table 2 and Figure 1 depict some ice-phase reactions that have been proposed to lead to the formation of ethanolamine on the surface of dust grains (S. Charnley 2001; D. E. Woon 2002; A. Singh et al. 2013; V. Wakelam et al. 2015; M. Ruaud et al. 2016; S. V. Kameneva et al. 2017; T. Suzuki et al. 2018; S. A. Krasnokutski 2021; V. M. Rivilla et al. 2021; G. Molpeceres & V. M. Rivilla 2022). The radical–radical (RR) reactions can happen without any activation barrier, whereas the neutral–radical (NR) reactions have to overcome a finite amount of energy barrier to start. We calculate this ice-phase activation barrier with ZPE correction using the QST2 method by finding a transition state structure with the DFT-B3LYP/6-31+G(d,p) level of theory. Table 2 also shows the ice-phase reaction enthalpies (using the same level of theory) to check whether the reactions are exothermic or endothermic. A continuum solvation field is considered to represent the ice features. The integral

equation formalism variant of the polarizable continuum model as a default self-consistent reaction field method is employed with water as a continuous homogeneous dielectric medium representing the solvent (E. Cancès et al. 1997; J. Tomasi et al. 2005).

2.2.3. Chemical Modeling

The Chemical Model of Molecular Cloud code (A. Das et al. 2015; P. Gorai et al. 2017a, 2017b; M. Sil et al. 2018; A. Das et al. 2019; P. Gorai et al. 2020; A. Das et al. 2021; M. Sil et al. 2021; B. Bhat et al. 2022; S. Srivastav et al. 2022; K. Taniguchi et al. 2023) is implemented for studying the formation of ethanolamine. It is a time-dependent gas-grain code that considers gas and homogeneous reactive ice mantle, i.e., a two-phase model, based on the rate equation approach.

Here, the gas-phase pathways are mainly adopted from the UMIST Database for Astrochemistry 2022 (T. J. Millar et al. 2024). Additionally, the destruction of gas-phase ethanolamine and its related species by major ions (H₃⁺, HCO⁺, H⁺, C⁺, He⁺ with a typical rate constant of $\sim 10^{-9}$ cm³ s⁻¹) and photoreactions are considered (see the Appendix). Altogether, our gas-phase network contains ~ 8848 reactions between ~ 750 species. A typical cosmic-ray ionization rate of the ISM $\sim 1.3 \times 10^{-17}$ s⁻¹ is considered. A typical ratio between the desorption and diffusion energy of ~ 0.5 is considered. Here, the surface chemistry network is primarily considered from M. Ruaud et al. (2016), and the BE of the surface species is considered from R. T. Garrod (2013), V. Wakelam et al. (2017), A. Das et al. (2018), M. Sil et al. (2021), S. K. Mondal et al. (2021), S. Srivastav et al. (2022). The BE set used in this work is available online.¹³ Additionally, the ice-phase reaction network contains other pathways used in A. Belloche et al. (2014), R. T. Garrod et al. (2017) regarding the H abstraction reactions. Moreover, we incorporate the ice-phase reactions detailed in Table 2 and Figure 1 and the BE reported in Table 1. Altogether our present surface network contains 1485 reactions and ~ 500 ice-phase species. Various ice-phase desorption mechanisms (thermal, cosmic-ray induced, reactive, and photodesorption) have been considered for the desorption of the newly included species. The encounter desorption (U. Hincelin et al. 2015; Q. Chang et al. 2021; A. Das et al. 2021) effect is considered to avoid overestimating the H₂ abundance on the grain surface. Recently, Y. Oba et al. (2019) and K. Furuya et al. (2022) estimated the reactive desorption probability of H₂S and PH₃ as $\sim 3\%$ – 4% . However, due to our limited understanding of this parameter, a typical value of ~ 0.01 is adopted (R. T. Garrod 2013; K. Furuya et al. 2015; A. Das et al. 2021). Typically, low metal abundances are used for this type of model. Currently, we are utilizing the values used by R. T. Garrod (2013) for a similar model, which is based on the initial low metal elemental abundance set by T. E. Graedel et al. (1982), except for He, C⁺, N, and O, for which values were derived from their diffuse cloud model. In this context, initial H, H₂, He, N, and O are considered neutral, while all other species are in their ionized form. The initial electron abundance is set equal to the total initial elemental abundances of positive ions.

Here, a physical condition is used (see Table 3), which is suitable to explain the environment corresponding to the surroundings of high-mass and low-mass protostars, i.e., hot

¹³ <https://www.iases.org.in/Ankan-web/AD-doc/BE-astrochem-kol-ver1.dat>

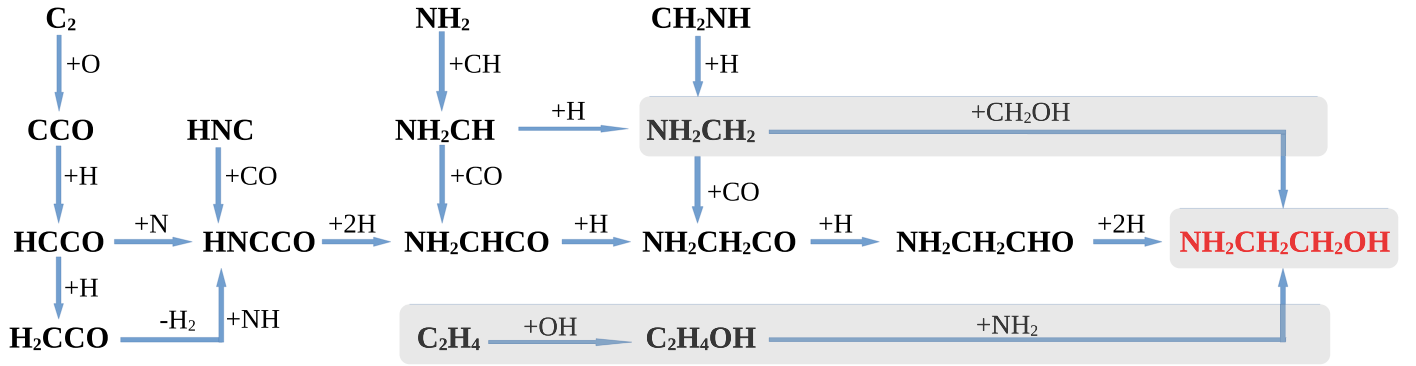


Figure 1. Summary of proposed chemical routes leading to the formation of ethanolamine on dust grain surfaces. The gray-shaded area corresponds to the most viable ice-phase routes for the formation of ethanolamine according to the chemical model presented here. Only the formation of ice-phase ethanolamine is emphasized here. We note that the destruction by major ions and UV photons (including cosmic-ray-induced ones) is not shown in this diagram, but they are considered in the chemical models.

Table 2
Ice-phase Reaction Pathways Related to the Formation of Ethanolamine Studied Using the DFT-B3LYP/6-31+G(d,p) Level of Theory

Reaction Number (Type)	Ice-phase/Grain-surface Reactions	Reaction Enthalpy (kcal mol ⁻¹)	Types of Reaction	Activation barrier (K)	References and Comments
R1 (RR)	C ₂ + O → CCO	-147.46 ^a	Exothermic	...	KIDA
R2 (RR)	H + CCO → HCCO	-123.88 ^a	Exothermic	...	KIDA, V. Wakelam et al. (2015)
R3 (RR)	H + HCCO → H ₂ CCO	-104.18 ^a	Exothermic	...	KIDA
R4	H ₂ CCO + NH → HNCCO + H ₂	-72.72 ^a	Exothermic	...	V. M. Rivilla et al. (2021)
R5 (RR)	HCCO + N → HNCCO	-169.75 ^a	Exothermic	...	S. Charnley (2001)
R6 (NN)	HNC + CO → HNCCO	22.60 ^a	Endothermic ^b	13289 ^{a,b}	S. V. Kameneva et al. (2017)
R7a (NR)	HNCCO + H → NH ₂ CCO	-71.99 ^a	Exothermic	3000 ^c	V. M. Rivilla et al. (2021)
R7b (RR)	NH ₂ CCO + H → NH ₂ CHCO	-77.64 ^a	Exothermic	...	V. M. Rivilla et al. (2021)
R8 (RR)	NH ₂ + CH → NH ₂ CH	-127.64 ^a	Exothermic	...	A. Singh et al. (2013)
R9 (RR)	NH ₂ CH + CO → NH ₂ CHCO	-26.33 ^a	Exothermic	...	A. Singh et al. (2013)
R10a (NR)	NH ₂ CHCO + H → NH ₂ CH ₂ CO	-51.17 ^a	Exothermic	3000 ^c	V. M. Rivilla et al. (2021)
R10b (RR)	NH ₂ CH ₂ CO + H → NH ₂ CH ₂ CHO	-89.46 ^a	Exothermic	...	V. M. Rivilla et al. (2021)
R11 (RR)	NH ₂ CH + H → NH ₂ CH ₂	-72.15 ^a	Exothermic	...	V. M. Rivilla et al. (2021)
R12 (NR)	CH ₂ NH + H → NH ₂ CH ₂	-40.78 ^a	Exothermic	2134 ^d	D. E. Woon (2002)
R13 (NN)	NH ₂ CH ₂ + CO → NH ₂ CH ₂ CO	-5.35 ^a	Exothermic	4227 ^c	A. Singh et al. (2013)
R14a (NR)	NH ₂ CH ₂ CHO + H → NH ₂ CH ₂ CH ₂ O	-21.25 ^a	Exothermic	2369 ^a	V. M. Rivilla et al. (2021)
R14b (RR)	NH ₂ CH ₂ CH ₂ O + H → NH ₂ CH ₂ CH ₂ OH	-102.00 ^a	Exothermic	...	V. M. Rivilla et al. (2021)
R15a (NR)	NH ₂ CH ₂ CHO + H → NH ₂ CH ₂ CHOH	-30.85 ^a	Exothermic	3236 ^a	V. M. Rivilla et al. (2021)
R15b (RR)	NH ₂ CH ₂ CHOH + H → NH ₂ CH ₂ CH ₂ OH	-92.40 ^a	Exothermic	...	V. M. Rivilla et al. (2021)
R16 (RR)	NH ₂ CH ₂ + CH ₂ OH → NH ₂ CH ₂ CH ₂ OH	-72.00 ^a	Exothermic	...	V. M. Rivilla et al. (2021)
R17 (NR)	C ₂ H ₄ + OH → C ₂ H ₄ OH	-27.5 ^f	Exothermic	710 ^f	G. Molpeceres & V. M. Rivilla (2022)
R18 (RR)	C ₂ H ₄ OH + NH ₂ → NH ₂ CH ₂ CH ₂ OH	-79.81	Exothermic	...	G. Molpeceres & V. M. Rivilla (2022)

Notes.

^a Calculated in this work.

^b Due to the high endothermicity of this reaction, it is not considered in our network.

^c Assumed in this work.

^d D. E. Woon (2002).

^e A. Singh et al. (2013).

^f G. Molpeceres & V. M. Rivilla (2022).

core and hot corino, respectively. The physical condition of our model is divided into three distinct stages: collapse, warm-up, and post-warm-up. During the warm-up stage, the collapse halts, and dust and gas temperatures gradually increase. The

timescale of this phase is primarily based on the approach of S. Viti et al. (2004), who used the observed protostellar luminosity function of S. Molinari et al. (2000) to derive effective temperatures throughout the accretion phase of a

Table 3
Adopted Physical Parameters Considered in Our Model

	Hot Core	Hot Corino
Collapse Phase		
t_{coll} (yr)	10^5	10^6
n_{Hmin} (cm^{-3})	3.0×10^3	3.0×10^3
n_{Hmax} (cm^{-3})	10^7	10^7
T_{gas} (K)	20	20
A_V	$A_{V0}(n_{\text{H}}/n_{\text{Hmin}})^{2/3}$ ($A_{V0} = 2$)	$A_{V0}(n_{\text{H}}/n_{\text{Hmin}})^{2/3}$ ($A_{V0} = 2$)
T_{ice} (K)	A. Zucconi et al. (2001), R. T. Garrod (2008)	A. Zucconi et al. (2001), R. T. Garrod (2008)
1st Warm-up Phase		
t_{warm1} (yr)	5.0×10^4	10^6
n_{H} (cm^{-3})	10^7	10^7
$T_{\text{gas,min}}$ (K)	20	20
$T_{\text{gas,max}}/T_{\text{ice,max}}^{\text{b}}$ (K)	200	200
$T_{\text{ice,min}}$ (K)	$T_{\text{ice,min}}^{\text{a}}$	$T_{\text{ice,min}}^{\text{a}}$
A_V	$A_{V\text{max}}^{\text{a}}$	$A_{V\text{max}}^{\text{a}}$
2nd Warm-up Phase		
t_{warm2} (yr)	2.1×10^4	4.3×10^5
n_{H} (cm^{-3})	10^7	10^7
$T_{\text{gas,min}}/T_{\text{ice,min}}$ (K)	200	200
$T_{\text{gas,max}}/T_{\text{ice,max}}^{\text{b}}$ (K)	400	400
A_V	$A_{V\text{max}}^{\text{a}}$	$A_{V\text{max}}^{\text{a}}$
Post-warm-up Phase		
t_{pw} (yr)	10^5	10^5
n_{H} (cm^{-3})	10^7	10^7
T_{gas} (K)	400	400
T_{ice} (K)	400	400
A_V	$A_{V\text{max}}^{\text{a}}$	$A_{V\text{max}}^{\text{a}}$
Total simulation time	2.712×10^5	2.53×10^6

Notes.

^a Obtained at the end of the collapsing phase.

^b A linear relationship between the temperature increase and time is being considered.

central protostar until it reaches the zero-age main sequence. They approximated the compelling temperature profile as a power law concerning the protostar's age. They used contraction times determined by P. A. Bernasconi & A. Maeder (1996) to estimate a timescale of 10^4 – 10^6 yr for stars of 60–65 solar masses, respectively. The physical parameters adopted in our model are summarized in Table 3 and Figure 2. Similar physical parameters were adopted in some of the earlier studies (R. T. Garrod & E. Herbst 2006; R. T. Garrod 2013; R. T. Garrod et al. 2017; P. Gorai et al. 2020; S. K. Mondal et al. 2021; S. Srivastav et al. 2022; K. Taniguchi et al. 2023).

2.2.4. Microwave Rotational Spectroscopy

Several of the proposed precursors of ethanolamine have not had their rotational spectroscopy measured (see Figure 1). Therefore, we are presenting the theoretical calculations of its dipole moments and rotational constants to aid future laboratory experiments. Rotational spectroscopy is the primary tool to detect species in the ISM. Almost 80% of the observed species having permanent electric dipole moments are detected

from their rotational transitions (B. A. McGuire 2022). The intensity of any rotational transition is directly and inversely proportional to the square of the dipole moment and the rotational partition function, respectively. Dipole moment components along the inertial axis and total dipole moments of ethanolamine and related molecules (HNCCO, NH_2CHCO , and $\text{NH}_2\text{CH}_2\text{CO}$, for which no data were available in the literature) calculated using the DFT-B3LYP/6-311++G(d,p) level of theory are summarized in Table 4. In accordance with the experimental work by R. E. Penn & R. F. Curl (1971), a very strong a-type dipole moment for ethanolamine is obtained, while the b-type and c-type lines are generally much weaker, indicating that ethanolamine has a predominant dipole moment along one principal axis, which has implications for its spectroscopic properties and structural characteristics. However, we note some deviations in the dipole moments compared to the values reported by R. E. Penn & R. F. Curl (1971). This suggests that employing a high-cost functional and basis set combination could help reduce these deviations, which is beyond the scope of this work. The values obtained by R. E. Penn & R. F. Curl (1971) for ethanolamine are based on experiments and could be considered more accurate. Our calculated dipole moments for HNCCO, NH_2CHCO , and $\text{NH}_2\text{CH}_2\text{CO}$ are relatively high (see Table 4), which would help to detect the molecules once the rotational spectroscopy is measured in the future.

The ground vibrational (A_0, B_0, C_0) and equilibrium (A_e, B_e, C_e) values of rotational constants and asymmetrically reduced quartic centrifugal distortion constants ($D_N, D_K, D_{NK}, d_N, d_K$) are also calculated for these species using the same level of theory and noted in Table 5. The percentage deviations of the rotational constants A, B, and C calculated in our work compared to those in R. E. Penn & R. F. Curl (1971) are underpredicted by 0.33%, 0.14%, and 0.39%, respectively. These small percentage deviations indicate a high degree of consistency between the two sets of results. Based on this, we provide the rotational spectroscopic constants for its related species, HNCCO, NH_2CHCO , and $\text{NH}_2\text{CH}_2\text{CO}$, for which no values were available in the literature.

3. Results and Discussion

3.1. Experimental Results

3.1.1. VUV Spectra of Pure Ethanolamine Ice

Figure 3 presents the stacked temperature-dependent VUV spectra of ethanolamine ice deposited at 10 K in the 120–230 nm range and subsequently warmed to higher temperatures.

At 10 K, we observe that the spectrum has a weak band/bump between 141 and 157 nm, and beyond 210 nm, there is no absorption. When warmed to higher temperatures, the spectra show no noticeable changes in the spectra until 100 K. On warming the ice to 130 K, we could observe that the band centered around 142 nm became more prominent while the peak positions remained unchanged. On further warming to 180 K, the spectrum peaked at 172 nm. At 180 K, the infrared red spectrum reveals an onset phase change. The two distinct bands could be due to the dimer, monomer forms of the ethanolamine, as mentioned earlier in the case of formamide ice (B. Sivaraman et al. 2012). Upon warming to 200 K, spectra recorded clearly show a completely crystalline phase, and beyond 210 K, the ice sublimates.

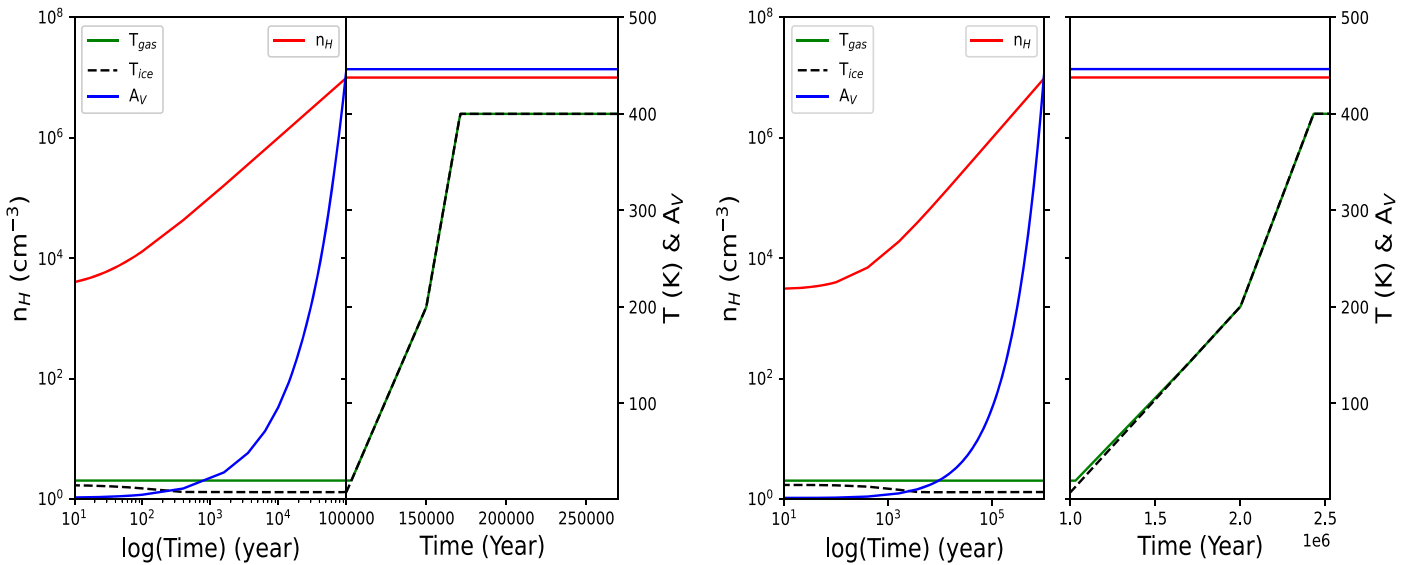


Figure 2. Adopted physical conditions for the hot core (left panel) and hot corino (right panel) regions.

Table 4

Dipole Moments Using the DFT-B3LYP/6-311++G(d,p) Level of Theory

Species	Dipole Moments (in D)			
	μ_a	μ_b	μ_c	μ_{tot}
HNCCO	1.15	0.82	0.00	1.42
NH ₂ CHCO	-2.24	1.41	0.00	2.65
NH ₂ CH ₂ CO	-2.57	1.45	1.24	3.20
NH ₂ CH ₂ CH ₂ OH	-3.00	1.14	0.55	3.25
	(2.65) ^a	(0.89) ^a	(0.42) ^a	(2.82) ^a

Note.

^a Absolute values of the total dipole moment and its components predicted by R. E. Penn & R. F. Curl (1971).

3.1.2. IR Spectra of Pure Ethanolamine Ice

Figure 4 depicts the temperature-dependent stacked IR spectra of ethanolamine ice deposited at 7 K between 3600 and 750 cm^{-1} . When deposited at 7 K, several peaks are noticed in two regions, one between 3600 and 2500 cm^{-1} and the other between 1700 and 800 cm^{-1} . The first column of Table 6 presents the positions of all these observed peaks. In the absence of any previous ice-phase spectra, comparing this with the previous liquid-phase and gas-phase results, the peak positions of pure ethanolamine at 10 K are in good agreement with that of the pure liquid phase of P. Jackson et al. (2009), and also with their theoretical gas-phase values. We see no significant difference up to 180 K after heating to higher temperatures. At 180 K, we see clear evidence of compaction of the ethanolamine ice, and when kept at 180 K for about 25 minutes, the phase change (amorphous/metastable to crystalline) is noticed. When this spectrum (isotherm at 180 K for 25 minutes spectrum of Figure 4) is compared with other spectra at lower temperatures, many additional peaks and sharper peaks are noticed. These are a result of the reorientation of ethanolamine molecules in the ice. The ice wholly sublimated at 230 K.

Another exciting aspect of ethanolamine ice is its dependence on the thickness of the ice. The upper panel of Figure 5 illustrates the deposition of ethanolamine ice at 7 K, while the

lower panel displays it for 190 K. The observation indicates that at the lower deposition temperature, several additional peaks (indicated by arrows in the upper panel of Figure 5) are present for the thick ice, which were absent in the thin ice.

A more detailed and quantitative study is needed to understand the origin and assignments for these peaks; nonetheless, it is a noteworthy observation. At 190 K (lower panel of Figure 5), evidence of phase change is noticed in almost all the new peaks in the thick ice at 7 K. Since some regions are already saturated, all the peaks are not seen. To further understand the behavior of ethanolamine ices, we performed several cycles of experiments by changing different variables like deposition temperature, deposition time, isotherm temperature, and isotherm time, a few results of which are shown in Table 7. From a series of experiments summarized in Table 7, we can infer that irrespective of the deposition time or rate of warming, the phase change temperature remains the same (190 K) when the ethanolamine ice is deposited at 7 K. The same ice deposited at 7 K, when kept at isotherm at 180 K for ~ 4 hr, changes from amorphous to crystalline at 180 K itself. However, when kept at isotherm at 170 K, the phase change does not occur even after 7 hr. This shows that the phase change process initiates around 175 K, but it is a slow process and hence requires more energy, which it could either get from higher thermal energy (higher temperature) or cumulative energy due to isotherm at any temperature above 175 K.

3.2. Computational Results

3.2.1. Chemical Modeling of Hot Core

Our quantum chemical calculations have revealed that all the reactions mentioned in Table 2 are exothermic. Among these reactions, the NR reactions possess activation barriers. These activation barriers have been estimated and directly incorporated into our model. In addition, some other reactions are presented based on our study. For the ice-phase synthesis of H₂CCO, the barrierless reactions R1–R3 are considered from KIDA. S. Charnley (2001) proposed the formation of HNCCO by the reaction between HCCO and N (reaction R5). This RR reaction can happen at each encounter without any activation barrier. It is noticed that this reaction is

Table 5
Ground Vibrational and Equilibrium Rotational Constants and Asymmetrically Reduced Quartic Centrifugal Distortion Constants of HNCCO, NH₂CHCO, NH₂CH₂CO, and NH₂CH₂CH₂OH with the DFT-B3LYP/6-311++G(d,p) Level of Theory

Sl. No.	Species	Rotational Constants	Calculated Values (in MHz)	Distortion Constants	Calculated Values (in MHz)
1.	HNCCO (Singlet)	A_0	268915.214	D_N	-0.00039892657
		B_0	4499.747	D_K	-1034.5240
		C_0	4367.401	D_{NK}	-2.4075581
		A_e	219743.385	d_N	0.00011340140
		B_e	4476.900	d_K	-0.58283144
		C_e	4387.512
2.	NH ₂ CHCO (Singlet)	A_0	43671.751	D_N	-0.0022392657
		B_0	4608.267	D_K	-0.71283617
		C_0	4283.586	D_{NK}	-0.16315747
		A_e	44190.690	d_N	-0.00078731244
		B_e	4634.836	d_K	-0.015381555
		C_e	4292.983
3.	NH ₂ CH ₂ CO (Doublet)	A_0	42231.836	D_N	-0.001274949
		B_0	4232.048	D_K	-0.73808078
		C_0	3984.143	D_{NK}	-0.0060688055
		A_e	42425.597	d_N	-0.000071558688
		B_e	4264.891	d_K	-0.0090472182
		C_e	4019.650
4.	NH ₂ CH ₂ CH ₂ OH (Singlet)	A_0	14401.029	D_N	-0.0061629178
		B_0	5429.504	D_K	-0.048060075
		C_0	4479.870	D_{NK}	0.020970813
		A_e	14460.409 (14508.73 ± 0.1 ^a)	d_N	-0.0018253369
		B_e	5538.498 (5546.46 ± 0.04 ^a)	d_K	-0.011234133
		C_e	4552.708 (4570.46 ± 0.03 ^a)

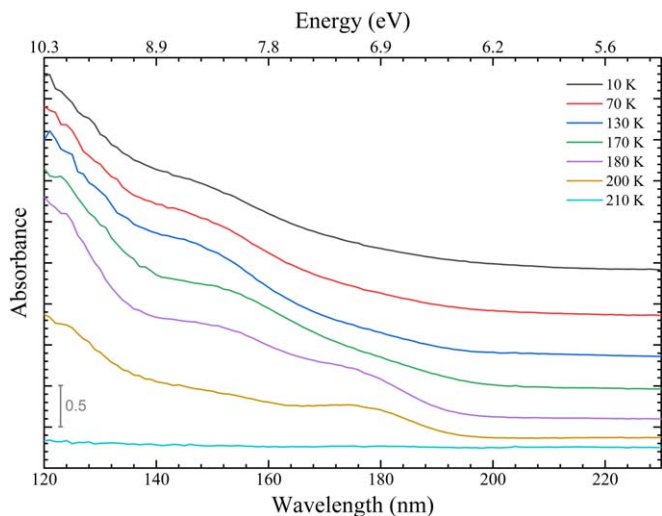
Note.^a R. E. Penn & R. F. Curl (1971)

Figure 3. Experimental VUV spectra of ethanolamine ices (stacked) in the 120–240 nm range for a selected set of temperatures.

exothermic, having a reaction enthalpy of $-169.75 \text{ kcal mol}^{-1}$. V. M. Rivilla et al. (2021) proposed reaction R4 for the formation of HNCCO. S. V. Kameneva et al. (2017) suggested the neutral–neutral (NN) reaction between HNC and CO (reaction R6). However, our calculation exhibits it as an endothermic reaction ($22.60 \text{ kcal mol}^{-1}$). Also, with the transition state calculation, it is noticed that it possesses a very high activation barrier ($\sim 13,289 \text{ K}$). In our reaction network, reaction R6 is not considered for forming HNCCO. Two

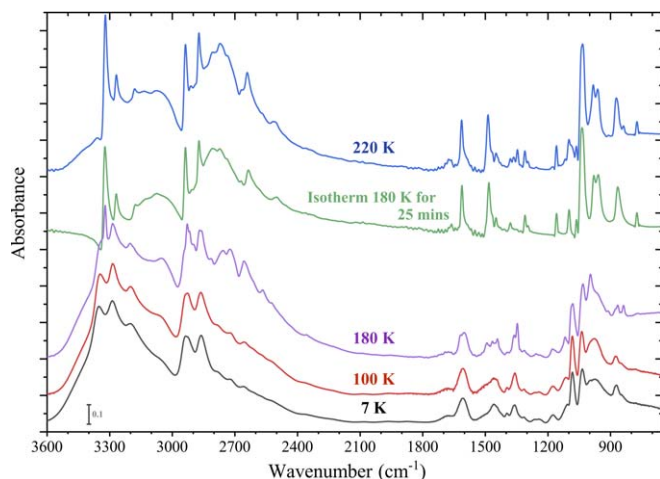


Figure 4. Temperature-dependent experimental IR spectra of ethanolamine ices.

successive hydrogenations of HNCCO are required to produce NH₂CHCO. The first step (R7a) is the NR reaction, and the second step (R7b) is the RR reaction. Both reactions are found to be exothermic. Since the second reaction is RR, it will process as barrierless. The first reaction should contain some activation barrier. However, an actual transition state of the reaction R7a is not obtained. Therefore, a conservative value of 3000 K is considered an educated estimation for the activation barrier of this reaction. The effect of this barrier is also discussed afterward.

Table 6

Comparing IR Peak Positions in the Ice Phase (From This Work) with That of the Previously Available in P. Jackson et al. (2009), Pure Liquid-phase Experiment and Theoretical Gas Phase and P. J. Krueger & H. D. Mettee (1965), in C₂Cl₄ Solution

This Work		Peak Position (cm ⁻¹)		
Experiment		Pure Liquid Phase	Previous Works	Theoretical Gas Phase
7 K	180 K	P. Jackson et al. (2009)	in C ₂ Cl ₄ Solution P. J. Krueger & H. D. Mettee (1965)	P. Jackson et al. (2009)
...	3640	3644
...	3624	3612
...	3526	3508
...	3411	...
3352	3314	3355	3340	...
3287	3268	3293
3201	3182
...	3136	3036
...	3073	2995
2936	2911	2927	...	2956
2861	2874	2864	...	2948
2786	2768
2726	2735
2658	2670
...	2642
...	2567
...	2513
1684	1674	1672
1606	1615	1601
1460	1489	1461	...	1465
...	1452
1395	1385	1405
1360	1362	1355
...	1348
...	1310
...	1294
1254	1257
1174	1160	1172	...	1198
1083	1119	1081
...	1101	1101
...	1066	1060
1035	1030	1033
...	986	999
970	962
872	874
...	839
...	774

There are other alternative pathways to form NH₂CHCO by the reactions R8 and R9 (A. Singh et al. 2013). Both these RR reactions are barrierless and exothermic. Therefore, these pathways are also considered in our network. NH₂CHCO is further processed through two successive hydrogenations (R10a and R10b) to form NH₂CH₂CHO. The first reaction (R10a) should contain the activation barrier. However, we could not get an actual transition state and consider the 3000 K barrier for R10a. At the same time, the second RR reaction, R10b, is barrierless and can be processed without an activation barrier.

The reactions R11–R13 provide another alternative formation pathway for NH₂CH₂CO, where R11 is RR barrierless exothermic reaction and R12 is NR exothermic possessing a barrier of 2134 K (D. E. Woon 2002). Following A. Singh et al.

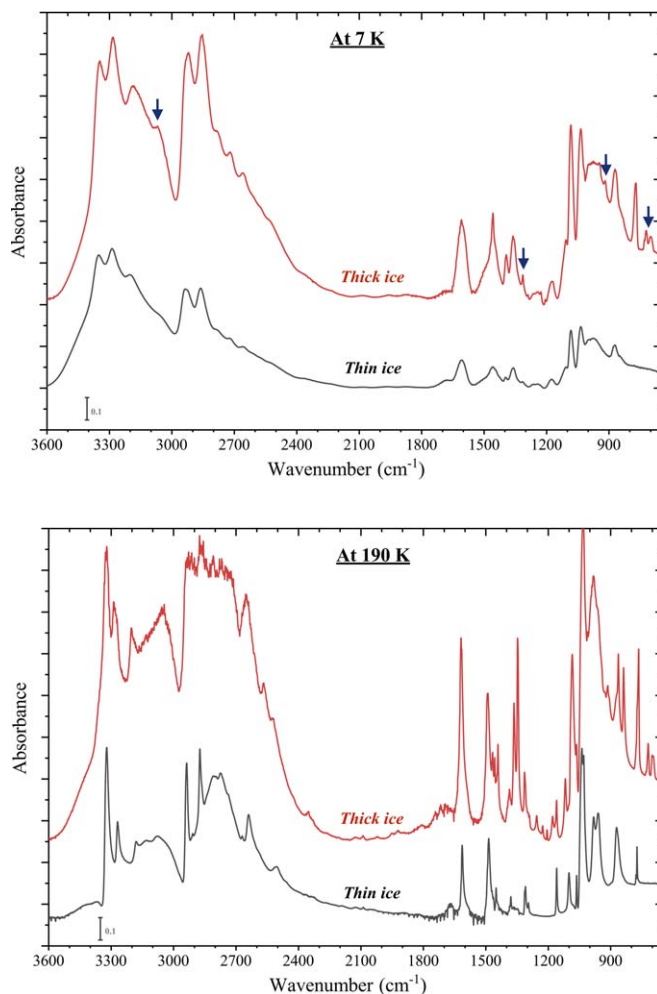


Figure 5. Comparison of experimental IR spectra of thin and thick ethanolamine ices at 7 K (upper panel) and after warming to 190 K (lower panel). The additional peaks in thick ice appearing at 7 K have been marked with blue arrows.

(2013), we consider the ice-phase NN reaction R13 with an activation barrier 4227 K. Hydrogenation of NH₂CH₂CHO can happen in two possible locations (C or O atom positions) and form NH₂CH₂CH₂O (R14a) or NH₂CH₂CHOH (R15a). Quantum chemical calculations yield activation barriers of 2369 K and 3236 K for R14a and R15a, respectively. NH₂CH₂CH₂O and NH₂CH₂CHOH further react with another hydrogen atom and form the target product ethanolamine (reactions R14b and R15b). Both of these RR reactions are found to be exothermic. The exothermic reaction R16 between two radicals NH₂CH₂ and CH₂OH to form ethanolamine as proposed by V. M. Rivilla et al. (2021) is included in our network. Recently, G. Molpeceres & V. M. Rivilla (2022) proposed two subsequent surface reactions in forming ethanolamine by C₂H₄ + OH → C₂H₄OH (R17, NR reaction) and C₂H₄OH + NH₂ → NH₂CH₂CH₂OH (R18, RR reaction). Furthermore, we consider an additional ice-phase barrierless reaction between NH₂CH₂CH₂OH and HCOOH for the formation of β-alanine.

Figure 6 shows the abundances of ethanolamine along with some of its related species (HNCCO, H₂CCO, CH₂OH, NH₂CH₂, and C₂H₄OH) obtained from our model. The lower X-axis in Figure 6 shows the time, the upper X-axis shows gas temperature, and the Y-axis represents the abundance with

Table 7
Log of IR Experiments Carried Out at Different Temperatures and Thicknesses and Different Isotherm Temperatures and Durations

Dep. Temp. (K)	Dep. Time (s)	Phase Change (K)	Ramp Rate (K minute ⁻¹)	Sublimation (K)	Isothermal Temp. and Duration	Remarks
7	220	190	10	235 – 240
7	903	190	5	230
7	425	190	5	230
7	435	180	5	230	180 K, 4 hr	Crystalline within 4 hr of isothermal at 180 K
170	2400	190	5	230	170 K, 7 hr	Compaction after 2 hr, no crystallization even after 7 hr
175	1500	175	5	220	175 K, 90 minutes	Ice turned crystalline
180	1200	180	5	230	...	Fully crystalline ice

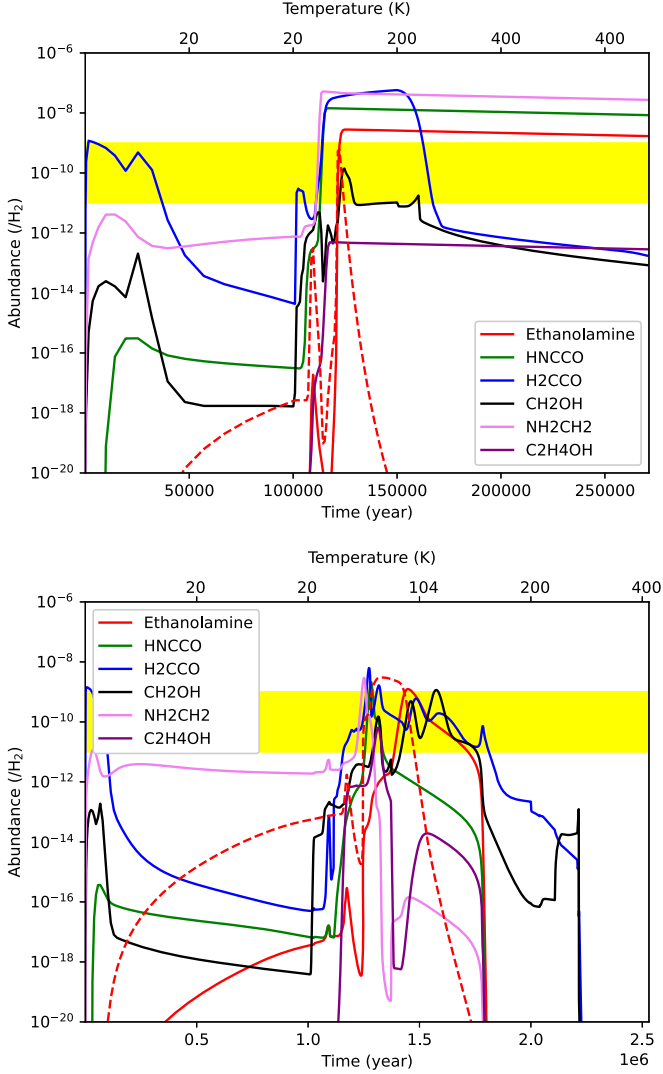


Figure 6. Time evolution of the ethanolamine abundances and some related species (HNCCO, H₂CCO, CH₂OH, NH₂CH₂, C₂H₄OH) for the hot core (upper panel) and hot corino region (lower panel). The dashed line represents the ice-phase ethanolamine abundance.

respect to H₂. The upper and lower panels represent the time evolution of abundances for the hot core and hot corino regions, respectively. Dashed lines show the abundance of ethanolamine in the absence of the reaction R16. Since the hydrogenation reaction by physisorption is not generally efficient beyond 20 K, we find a significant contribution of ethanolamine by the surface reaction between CH₂OH and

NH₂CH₂ (reaction R16). In the absence of reaction number R16, ethanolamine formation is dominated by another surface reaction between C₂H₄OH and NH₂ (reaction number R18).

In the case of a hot core, we consider a fast collapsing and a fast warm-up timescale. The upper panel of Figure 6 shows that a peak abundance of $\sim 2.8 \times 10^{-9}$ could be achieved around 100 K for a hot core region. We notice that most of the ice-phase formation of ethanolamine happens here between 60 and 90 K (the red dashed line in Figure 6 depicts ice-phase ethanolamine). Due to a shorter warm-up timescale, its destruction would not have taken place for a long period; as a result, we can see a healthy abundance of ethanolamine at the end of the simulation. On the contrary, we consider a slow collapsing and warm-up timescale for the hot corino (lower panel of Figure 6). It shows a peak abundance of 1.2×10^{-9} around 90 K and then dramatically declines. It is worth noting that gas-phase ethanolamine production is predominantly influenced by ice-phase reaction R16 and its subsequent desorption.

We initially set the density at $3 \times 10^3 \text{ cm}^{-3}$ and utilized low metal initial abundances, typically considered the standard for hot core/corino models. To assess the impact of the initial density on our calculation, we also experimented with an initial density of 10^4 cm^{-3} . However, this alternative did not result in any noticeable deviation. This is because ethanolamine production is predominantly influenced during the warm-up phase when the density is 10^7 cm^{-3} .

3.3. Astronomical Implications

Ethanolamine has been only detected so far toward a molecular cloud in the Galactic center, G+0.693-0.027 (V. M. Rivilla et al. 2021), with an abundance compared to H₂ of $\sim 10^{-10}$. It has also been searched for toward star-forming regions, including several hot cores (S. L. Widicus et al. 2003; E. S. Wirström & P. Bergman 2007), and the prototypical hot corino IRAS 16293-2422 B (P. Nazari et al. 2024), but the molecule was not detected, allowing only for the computation of upper limits for its abundance. S. L. Widicus et al. (2003) used the 10 m telescope of the Caltech Submillimeter Observatory (CSO), and interferometric observations of the Owens Valley Radio Observatory (OVRO), while E. S. Wirström & P. Bergman (2007) used the Onsala 20 m telescope. To convert the column density upper limits reported in these works into abundances we have used the values observed toward Orion KL. For the single-dish observations, we have corrected the beam dilution since it is expected that the spatial extent of the ethanolamine is compact, as are other complex molecules. For the size of the emission and the associated value of $N(\text{H}_2)$ in the same volume, we have used the values derived for the Orion KL hot core by

S. Feng et al. (2015) and N. R. Crockett et al. (2014), which are, respectively, $10'' \times 10''$ and $3.1 \times 10^{23} \text{ cm}^{-2}$, and $3.49'' \times 2.57''$ and $2.3 \times 10^{24} \text{ cm}^{-2}$. We obtain that the CSO observations provide an upper limit for the abundance of ethanolamine of $<(1.3\text{--}1.8) \times 10^{-9}$, while the Onsala observations give slightly higher values of $<(4.1\text{--}5.8) \times 10^{-9}$. However, we note that these numbers should be taken with caution, given the uncertainties of the size and $N(\text{H}_2)$ assumptions. The OVRO observations of S. L. Widicus et al. (2003) were centered toward the Orion Compact Ridge, so in this case, we have used the size and $N(\text{H}_2)$ derived by S. Feng et al. (2015) in this source, which is $3.49'' \times 2.57''$ and $1.28 \times 10^{24} \text{ cm}^{-2}$, respectively. The beam of the observations was $6.8'' \times 4.8''$. After applying the beam dilution, we obtain an upper limit of ethanolamine abundance of $<1.8 \times 10^{-10}$, which is at least one order of magnitude lower than that derived from the single-dish observations and very similar to the value calculated by V. M. Rivilla et al. (2021) toward G+0.693. Therefore, deep searches of ethanolamine toward hot cores are needed to establish if it is equally abundant in G+0.693, or alternatively, this species has lower abundances in these environments. Our hot core model predicts a peak abundance of $\sim 2.8 \times 10^{-9}$. Moreover, P. Nazari et al. (2024) estimated an upper limit of ethanolamine column density $<6 \times 10^{14} \text{ cm}^{-2}$ toward IRAS 16293-2422 B using the Atacama Large Millimeter/submillimeter Array (ALMA). Considering a H_2 column density of $\sim 10^{25} \text{ cm}^{-2}$ (J. K. Jørgensen et al. 2016), it yields an upper limit of abundance $<6 \times 10^{-11}$. This indicates that the species is less abundant in this hot corino than in G+0.693. However, our hot corino model predicts a peak abundance of $\sim 1.2 \times 10^{-9}$. For the sake of simplicity, ethanolamine abundances in the surroundings of the hot core and hot corino region would vary between 10^{-11} and 10^{-9} . This limit is highlighted with the yellow horizontal bar in Figure 6. Since the nondetection of ethanolamine toward hot cores/corinos was possibly due to a lack of sensitivity, more high-sensitivity and high-resolution spectral data could lead to its future identification. Furthermore, the high line density in these hot environments might be contributing to preventing the detection of ethanolamine, since its weak expected lines can be severely blended by stronger lines from more abundant species. To alleviate this, searches at lower frequencies, for instance in the new ALMA band 3, might help.

Apart from star-forming regions, ethanolamine has been detected in the Almahata Sitta meteorite (D. P. Glavin et al. 2010). This suggests the presence of ethanolamine in solar system objects. The IR spectra presented for ethanolamine ices would help augment the JWST data toward understanding the origin of a phospholipid precursor in solar system objects.

4. Conclusion

Theoretical and experimental work has been conducted to comprehend the formation of ethanolamine and its photochemistry under interstellar conditions. The major conclusions of this work are highlighted below:

1. In this study, we present the first temperature-dependent VUV and mid-IR spectra of pure ethanolamine ices under astrochemical conditions. Our results show a close correspondence between the VUV and IR spectra in relation to phase change (occurring around 180 K) and sublimation (occurring around 230 K). We have observed

that the phase change is greatly influenced by the deposition temperature and the isothermal condition. The VUV and IR spectral features outlined in this paper can be valuable for its future identification of ethanolamine in the interstellar ices and other cold regions of planetary and cometary bodies.

2. Quantum chemical calculations are carried out to study the feasibility of ice-phase reactions involving the formation of ethanolamine. Some of these reactions contain activation barriers, which are estimated by our quantum chemical calculations. The obtained values are directly used in the model.
3. Ethanolamine formation in high-mass and low-mass star-forming regions is explored by chemical models. It depicts that the formation of ethanolamine by RR surface reactions in the warmer regions (60–90 K) is favorable. Our modeled abundances are consistent with the estimated upper limit of ethanolamine abundance in the hot core/corino surroundings.
4. To assist the interstellar search of several proposed precursors of ethanolamine (HNCCO, NH_2CHCHO , and $\text{NH}_2\text{CH}_2\text{CO}$), and to allow for a proper derivation of the column densities from observations, we have performed theoretical calculations to derive their dipole moments, and their rotational constants. Upon reassessing the calculated rotational constants for ethanolamine and aligning them with prior data (R. E. Penn & R. F. Curl 1971), we have extended our analysis to encompass the rotational and distortional constants for these species, which were absent in the literature.

Acknowledgments

We thank NSRRC for providing the beamtime and accessories that allowed us to perform the experiments. R.R., B.S., and N.J.M. are grateful to Sir John and Lady Mason Academic Trust for the support provided to carry out measurements at NSRRC. R.R., J.K.M., A.B., and B.S. acknowledge support from the Physical Research Laboratory (Department of Space, Government of India). R.R., J.K.M., and B.S. would also like to acknowledge the Interdisciplinary program for astrobiology & astrochemistry (IPAA) of the Physical Research Laboratory. AB was a J.C. Bose Fellow during the period of this work. P.J. would like to acknowledge the support of an INSA Senior Scientist Fellowship at PRL, Ahmedabad. N.J.M. acknowledges the receipt of funding from the Europlanet 2024 RI, which has been funded by the European Union Horizon 2020 Research Innovation Program under grant agreement No. 871149. M.S. acknowledges financial support through the European Research Council (consolidated grant COLLEXISM, grant agreement ID: 811363). A.D. acknowledges the support of Max-Planck-Institute for extraterrestrial Physics for sponsoring a scientific visit. V.M.R. acknowledges support from the grant PID2022-136814NB-I00 by the Spanish Ministry of Science, Innovation and Universities/State Agency of Research MICIU/AEI/10.13039/501100011033 and by ERDF, UE; the grant RYC2020-029387-I funded by MICIU/AEI/10.13039/501100011033 and by “ESF, Investing in your future,” and from the Consejo Superior de Investigaciones Científicas (CSIC) and the Centro de Astrobiología (CAB) through project 20225AT015 (Proyectos intramurales especiales del CSIC); and from the grant CNS2023-144464 funded by MICIU/AEI/

10.13039/501100011033 and by “European Union NextGenerationEU/PRTR.”


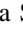

Appendix Gas-phase Destruction Reactions of Ethanolamine and Related Species

The following reactions are included in our network for destroying gas-phase ethanolamine and related species. The format of this reaction follows the standard UMIST 2022 network.



:IN:C+:C2H4OH:HCO+:C2H4:::1:1.00e-09:-
 0.50:0.0:10:41000:E:C::
 :CR:HNCCO:CRPHOT:NH:C2O:::1:1.30e-
 17:0.00:1500.0:10:41000:M:C
 :CR:NH2CCO:CRPHOT:NH2:C2O:::1:1.30e-
 17:0.00:1500.0:10:41000:M:C
 :CR:NH2CHCO:CRPHOT:NH3:C2O:::1:1.30e-
 17:0.00:1500.0:10:41000:M:C
 :CR:NH2CH2CO:CRPHOT:NH2:CH2CO:::1:1.30e-
 17:0.00:1500.0:10:41000:M:C
 :CR:NH2CH2CHO:CRPHOT:NH2:CH2CHO:::1:1.30e-
 17:0.00:1500.0:10:41000:M:C
 :CR:NH2CH2CH2O:CRPHOT:NH2:CH3CHO:::1:1.30e-
 17:0.00:1500.0:10:41000:M:C
 :CR:NH2CH2CH2OH:CRPHOT:NH3:CH3CHO:::1:1.30e-
 17:0.00:1500.0:10:41000:M:C
 :CR:NH2C2H3OH:CRPHOT:NH2:CH3CHO:::1:1.30e-
 17:0.00:1500.0:10:41000:M:C
 :CR:NH2CH:CRPHOT:NH2:CH:::1:1.30e-
 17:0.00:1500.0:10:41000:M:C
 :CR:NH2CH2:CRPHOT:NH2:CH2:::1:1.30e-
 17:0.00:1500.0:10:41000:M:C
 :CR:C3H7NO2:CRPHOT:H2:CH3CHO:HNCO:::1:1.30e-
 17:0.00:1500.0:10:41000:M:C
 :CR:C2H4OH:CRPHOT:C2H4:OH:::1:1.30e-
 17:0.00:1500.0:10:41000:M:C
 :PH:HNCCO:PHOTON:NH:C2O:::1:1.00e-
 10:0.00:2.0:10:41000:M:C
 :PH:NH2CCO:PHOTON:NH2:C2O:::1:1.00e-
 10:0.00:2.0:10:41000:M:C
 :PH:NH2CHCO:PHOTON:NH3:C2O:::1:1.00e-
 10:0.00:2.0:10:41000:M:C
 :PH:NH2CH2CO:PHOTON:NH2:CH2CO:::1:1.00e-
 10:0.00:2.0:10:41000:M:C
 :PH:NH2CH2CHO:PHOTON:NH2:CH2CHO:::1:1.00e-
 10:0.00:2.0:10:41000:M:C
 :PH:NH2CH2CH2O:PHOTON:NH2:CH3CHO:::1:1.00e-
 10:0.00:2.0:10:41000:M:C
 :PH:NH2CH2CH2OH:PHOTON:NH3:CH3CHO:::1:1.00e-
 10:0.00:2.0:10:41000:M:C
 :PH:NH2C2H3OH:PHOTON:NH2:CH3CHO:::1:1.00e-
 10:0.00:2.0:10:41000:M:C
 :PH:NH2CH:PHOTON:NH2:CH:::1:1.00e-
 10:0.00:2.0:10:41000:M:C
 :PH:NH2CH2:PHOTON:NH2:CH2:::1:1.00e-
 10:0.00:2.0:10:41000:M:C
 :PH:C3H7NO2:PHOTON:H2:CH3CHO:HNCO:::1:1.00e-
 10:0.00:2.0:10:41000:M:C
 :PH:C2H4OH:PHOTON:C2H4:OH:::1:1.00e-
 10:0.00:2.0:10:41000:M:C

ORCID iDs

R. Ramachandran  <https://orcid.org/0000-0002-4122-9501>
 Milan Sil  <https://orcid.org/0000-0001-5720-6294>
 Prasanta Gorai  <https://orcid.org/0000-0003-1602-6849>
 J. K. Meka  <https://orcid.org/0000-0003-0022-4226>
 Pavithra Sundararajan  <https://orcid.org/0000-0001-8809-7633>
 J.-I. Lo  <https://orcid.org/0000-0002-0153-1423>
 S.-L. Chou  <https://orcid.org/0000-0002-6528-3721>
 Y.-J. Wu  <https://orcid.org/0000-0001-9261-0655>

P. Janardhan  <https://orcid.org/0000-0003-2504-2576>
 B.-M. Cheng  <https://orcid.org/0000-0002-8540-6274>
 Anil Bhardwaj  <https://orcid.org/0000-0003-1693-453X>
 Víctor M. Rivilla  <https://orcid.org/0000-0002-2887-5859>
 N. J. Mason  <https://orcid.org/0000-0002-4468-8324>
 B. Sivaraman  <https://orcid.org/0000-0002-2833-0357>
 Ankan Das  <https://orcid.org/0000-0003-4615-602X>

References

- Altwegg, K., Balsiger, H., Bar-Nun, A., et al. 2016, *SciA*, **2**, e1600285
 Belloche, A., Garrod, R. T., Müller, H. S. P., & Menten, K. M. 2014, *Sci*, **345**, 1584
 Belloche, A., Menten, K. M., Comito, C., et al. 2008, *A&A*, **482**, 179
 Bernasconi, P. A., & Maeder, A. 1996, *A&A*, **307**, 829
 Bernstein, M. P., Dworkin, J. P., Sandford, S. A., Cooper, G. W., & Allamandola, L. J. 2002, *Natur*, **416**, 401
 Bhat, B., Gorai, P., Mondal, S. K., Chakrabarti, S. K., & Das, A. 2022, *AdSpR*, **69**, 415
 Boogert, A. C. A., Gerakines, P. A., & Whittet, D. C. B. 2015, *ARA&A*, **53**, 541
 Cancès, E., Mennucci, B., & Tomasi, J. 1997, *JChPh*, **107**, 3032
 Carrascosa, H., Cruz-Díaz, G. A., Muñoz Caro, G. M., Dartois, E., & Chen, Y.-J. 2020, *MNRAS*, **493**, 821
 Chang, Q., Zheng, X.-L., Zhang, X., et al. 2021, *RAA*, **21**, 039
 Charnley, S. 2001, in *The Bridge Between the Big Bang and Biology: Stars, Planetary Systems, Atmospheres, Volcanoes: Their Link to Life*, ed. F. Giovannelli (Rome: Consiglio Nazionale delle Ricerche), 139
 Crockett, N. R., Bergin, E. A., Neill, J. L., et al. 2014, *ApJ*, **787**, 112
 Cunningham, M. R., Jones, P. A., Godfrey, P. D., et al. 2007, *MNRAS*, **376**, 1201
 Das, A., Gorai, P., & Chakrabarti, S. K. 2019, *A&A*, **628**, A73
 Das, A., Majumdar, L., Sahu, D., et al. 2015, *ApJ*, **808**, 21
 Das, A., Sil, M., Ghosh, R., et al. 2021, *FrASS*, **8**, 78
 Das, A., Sil, M., Gorai, P., Chakrabarti, S. i. K., & Loison, J. C. 2018, *ApJS*, **237**, 9
 Dunning, T. H. J. 1989, *JChPh*, **90**, 1007
 Ehrenfreund, P., Bernstein, M. P., Dworkin, J. P., Sandford, S. A., & Allamandola, L. J. 2001, *ApJ*, **550**, L95
 Elowitz, M., Sivaraman, B., Hendrix, A., et al. 2021, *SciA*, **7**, eaba5749
 Elsila, J. E., Dworkin, J. P., Bernstein, M. P., Martin, M. P., & Sandford, S. A. 2007, *ApJ*, **660**, 911
 Feng, S., Beuther, H., Henning, T., et al. 2015, *A&A*, **581**, A71
 Fiore, M., Chieffo, C., Lopez, A., et al. 2022, *AsBio*, **22**, 598
 Frisch, M. J., Trucks, G. W., Schlegel, H. B., et al., 2013 Gaussian 09 Revision D.01, <https://gaussian.com/>
 Frisch, M. J., Trucks, G. W., Schlegel, H. B., et al., 2016 Gaussian16 Revision B.01, <https://gaussian.com/>
 Furuya, K., Aikawa, Y., Hincelin, U., et al. 2015, *A&A*, **584**, A124
 Furuya, K., Oba, Y., & Shimonishi, T. 2022, *ApJ*, **926**, 171
 Garrod, R. T. 2008, *A&A*, **491**, 239
 Garrod, R. T. 2013, *ApJ*, **765**, 60
 Garrod, R. T., Belloche, A., Müller, H. S. P., & Menten, K. M. 2017, *A&A*, **601**, A48
 Garrod, R. T., & Herbst, E. 2006, *A&A*, **457**, 927
 Germain, A., Tinacci, L., Pantaleone, S., Ceccarelli, C., & Ugliengo, P. 2022, *ESC*, **6**, 1286
 Glavin, D. P., Aubrey, A. D., Callahan, M. P., et al. 2010, *M&PS*, **45**, 1695
 Gorai, P., Bhat, B., Sil, M., et al. 2020, *ApJ*, **895**, 86
 Gorai, P., Das, A., Das, A., et al. 2017a, *ApJ*, **836**, 70
 Gorai, P., Das, A., Majumdar, L., et al. 2017b, *MolAs*, **6**, 36
 Graedel, T. E., Langer, W. D., & Frerking, M. A. 1982, *ApJS*, **48**, 321
 Heyl, J., Sellentin, E., Holdship, J., & Viti, S. 2022, *MNRAS*, **517**, 38
 Hincelin, U., Chang, Q., & Herbst, E. 2015, *A&A*, **574**, A24
 Jackson, P., Robinson, K., Puxty, G., & Attalla, M. 2009, *EnPro*, **1**, 985
 Jones, P. A., Cunningham, M. R., Godfrey, P. D., & Cragg, D. M. 2007, *MNRAS*, **374**, 579
 Jørgensen, J. K., van der Wiel, M. H. D., Coutens, A., et al. 2016, *A&A*, **595**, A117
 Kameneva, S. V., Tyurin, D. A., & Feldman, V. I. 2017, *PCCP*, **19**, 24348
 Krasnokutski, S. A. 2021, *LTP*, **47**, 199
 Krueger, P. J., & Mettee, H. D. 1965, *CajCh*, **43**, 2970
 Kuan, Y.-J., Charnley, S. B., Huang, H.-C., Tseng, W.-L., & Kisiel, Z. 2003, *ApJ*, **593**, 848

- Kvnevolden, K. A., Lawless, J. G., & Ponnampereuma, C. 1971, *PNAS*, **68**, 486
- Lu, H.-C., Chen, H.-K., Cheng, B.-M., & Ogilvie, J. F. 2008, *AcSpA*, **71**, 1485
- McGuire, B. A. 2022, *ApJS*, **259**, 30
- Millar, T. J., Walsh, C., Van de Sande, M., & Markwick, A. J. 2024, *A&A*, **682**, A109
- Molinari, S., Brand, J., Cesaroni, R., & Palla, F. 2000, *A&A*, **355**, 617
- Molpeceres, G., & Rivilla, V. M. 2022, *A&A*, **665**, A27
- Mondal, S. K., Gorai, P., Sil, M., et al. 2021, *ApJ*, **922**, 194
- Nazari, P., Cheung, J. S. Y., Ferrer Asensio, J., et al. 2024, *A&A*, **686**, A59
- Novakovskaya, Y. V., & Rodnikova, M. N. 2015, *Struct. Chem.*, **26**, 177
- Nuevo, M., Auger, G., Blanot, D., & d'Hendecourt, L. 2008, *OLEB*, **38**, 37
- Oba, Y., Tomaru, T., Kouchi, A., & Watanabe, N. 2019, *ApJ*, **874**, 124
- Penn, R. E., & Curl, R. F. 1971, *JChPh*, **55**, 651
- Ramachandran, R., Rahul, K. K., Meka, J. K., et al. 2023, *J. Chem. Sci.*, **135**, 77
- Redondo, P., Largo, A., & Barrientos, C. 2015, *A&A*, **579**, A125
- Rivilla, V. M., Jiménez-Serra, I., Martín-Pintado, J., et al. 2021, *PNAS*, **118**, e2101314118
- Rocha, W. R. M., Rachid, M. G., Olsthoorn, B., et al. 2022, *A&A*, **668**, A63
- Rnaud, M., Wakelam, V., & Hersant, F. 2016, *MNRAS*, **459**, 3756
- Sil, M., Gorai, P., Das, A., et al. 2018, *ApJ*, **853**, 139
- Sil, M., Roy, A., Gorai, P., et al. 2024, *A&A*, **690**, A252
- Sil, M., Srivastav, S., Bhat, B., et al. 2021, *AJ*, **162**, 119
- Singh, A., Shivani, M. A., & Tandon, P. 2013, *RAA*, **13**, 912
- Sivaraman, B., Raja Sekhar, B. N., Jones, N. C., Hoffmann, S. V., & Mason, N. J. 2012, *CPL*, **554**, 57
- Srivastav, S., Sil, M., Gorai, P., et al. 2022, *MNRAS*, **515**, 3524
- Suzuki, T., Majumdar, L., Ohishi, M., et al. 2018, *ApJ*, **863**, 51
- Taniguchi, K., Sanhueza, P., Olguin, F. A., et al. 2023, *ApJ*, **950**, 57
- Tinacci, L., Germain, A., Pantaleone, S., et al. 2022, *ESC*, **6**, 1514
- Tomasi, J., Mennucci, B., & Cammi, R. 2005, *ChRv*, **105**, 2999
- Viti, S., Collings, M. P., Dever, J. W., McCoustra, M. R. S., & Williams, D. A. 2004, *MNRAS*, **354**, 1141
- Wakelam, V., Loison, J. C., Hickson, K. M., & Ruaud, M. 2015, *MNRAS*, **453**, L48
- Wakelam, V., Loison, J.-C., Mereau, R., & Ruaud, M. 2017, *MolAs*, **6**, 22
- Widicus, S. L., Drouin, B. J., Dyl, K. A., & Blake, G. A. 2003, *JMoSp*, **217**, 278
- Wirström, E. S., Bergman, P., Hjalmarson, Å., & Nummelin, A. 2007, *A&A*, **473**, 177
- Woon, D. E. 2002, *ApJL*, **571**, L177
- Zucconi, A., Walmsley, C. M., & Galli, D. 2001, *A&A*, **376**, 650